


## Mode competition in a plunging foil with an active flap: A multiscale modal analysis approach

Tso-Kang Wang and Kourosh Shoele <sup>\*</sup>

*Department of Mechanical Engineering, Joint College of Engineering Florida State University–Florida A&M University, Tallahassee, Florida 32310, USA*



(Received 24 September 2021; accepted 23 March 2022; published 12 April 2022)

Flow-induced fluttering has a significant role in aircraft stability, renewable energy extraction, animal locomotion, and many other applications. While being a ubiquitous phenomenon, the control of the flutter response has been primarily limited to simplified systems and, often, with the help of linear inviscid flow theories. In this paper, we numerically investigate how the plunging response of a foil can be regulated using an active flap to improve structural safety or enhance the energy extraction efficiency of the foil with a tightly coupled fluid-structure interaction algorithm. A broad range of foil and flap settings was tested, and their flow dynamics have been investigated. A multiscale modal analysis technique suitable for fluid-structure interaction systems is employed to systematically isolate the active flap-induced and flow-induced modes. It is observed that the competition between these two modes dictates the plunging response of the foil. The active flap can modulate the leading edge vortex shedding with larger flapping amplitude and regulate the foil heaving motion. The ratio of the competing modal energy is proposed to evaluate the control efficacy of the morphing surface, and the onset of the lock-in is associated with the ratio approaching unity. It is shown that the morphing flap is a good candidate for active flow control.

DOI: [10.1103/PhysRevFluids.7.044701](https://doi.org/10.1103/PhysRevFluids.7.044701)

### I. INTRODUCTION

Flow-induced flutter has been the subject of continual fluid dynamic research since the failed attempt to fly a monoplane by Samuel P. Langley in 1903. Bisplinghoff *et al.* [1] defined aeroelasticity as “the phenomenon which exhibits appreciable reciprocal interactions (static or dynamic) between aerodynamic forces and the deformations induced in the structure.” The physics of flow-induced flutter is composed of interactions between the flow and elastic or inertial structures [2]. Two primary mechanisms that specify the fluttering status of a foil are the coupling of the torsional and heaving modes of the airfoil and the flow separation and reattachment on the foil surface [3]. Under the right conditions, the fluttering response can lead to a self-sustained limit cycle oscillations and even cause instabilities [4–6]. In the case of instability, the fluttering motion due to the aeroelastic interaction presents a severe threat to the airfoil structural integrity. The aeroelastic instability has become even a more critical design factor with the development of faster and lighter airplanes [7,8]. Structures other than aerial systems can also be affected by aeroelasticity [9]. An example is the aeroelastic response of wind turbine blades in turbulent atmospheric flows [10]. Another famous instance is the collapse of the Tacoma Narrows bridge due to stall flutter [11].

Flow-induced elastic oscillation is also a critical physical mechanism in many biological systems. Oscillating foils are often applied as a prototype model of animal locomotion. For example, the

---

\*kshoele@eng.famu.fsu.edu

beating of the caudal fins of thunniform fishes such as tuna has been studied using pitching and heaving foil configurations [12–14]. The hovering motion of insects or miniature flying systems is often mathematically described with rapidly oscillating foil-shaped wings. This model has been adopted to study the efficiency of the flapping foils [15–19]. Similarly, in the past decade, the potentials of utilizing the flow-induced elastic response for energy harvesting have been explored for various conditions [20–22]. Energy-generating devices, such as a piezoelectric component attached to a foil, can harvest energy from the flow through the self-sustained vibration. Flapping foils as energy harvesters are environmentally friendly with fewer maintenance requirements and can be easily integrated into existing designs [23,24].

Different flow control techniques have been proposed to suppress the vibration or regularize the airfoil's dynamic stall response. Passive control methods have been suggested to suppress vibration. As an example among many other studies, Lee *et al.* [25] explored whether the redistribution of the mechanical energy with nonlinear energy sinks could postpone the cascade of heaving and pitching modes of the airfoil, and Fatimah *et al.* [26] demonstrated that the vibration of the structure could be alleviated by adjusting the stiffness between the oscillating object and an absorbing mass. Recently smart materials have been used to produce continuous surface deflection of an airfoil and modify aerodynamic characteristics of the system [27–29]. Although many diverse flow control techniques have been proposed, it is fair to say that conceivably, the most feasible engineering solution is still an active flap at the leading edge or trailing edge. Block *et al.* [30] employed Theodorsen's flow theorem [31] to identify a controlling action that can stabilize the system by adjusting the angle of the trailing edge flap. Wang *et al.* [32] further used a multi-input system with active control surfaces at both leading and trailing edges and designed a full-state feedforward/feedback controller with a high-gain observer. Experimentally, Platanitis *et al.* [33] employed a geometrically nonlinear controller designed via Lie algebraic methods on a dual-control surface airfoil to suppress the oscillation under optimal conditions. Medina *et al.* [34] experimentally investigated the physics of flow separation at the leading edges due to rapid trailing-edge flap deflection.

Many fundamental questions remain unsettled despite previous research on using control surfaces to modulate flow-induced flutter. The model-based control methods developed for active control surfaces are often centered around inviscid flow models such as Theodorsen's theory, in which a foil is represented with a two-dimensional inviscid plate [35–37]. These control algorithms consider the fluid-structure interaction (FSI) dynamics as a change in the flow momentum due to small-amplitude motion around the structure's mean position. Therefore, they cannot capture the flow change associated with the large structural deformation, unsteady vortex separations, and nonlinear vortex-body interaction. Furthermore, few reduced-order modeling techniques are available that simultaneously consider both structure and fluid responses. For example, Goza and Colonius [38] combined fluidic and structural energy to construct hybrid proper orthogonal decomposition (POD) modes to correlate the structural motion and the induced flow features. Liberge *et al.* [39] interpolate the time-variant grid to a fixed grid to perform POD on a global velocity field. Menon and Mittal [40] fixed the moving frame and correct the dynamic mode decomposition (DMD) modes with the frequency spectrum of the fixed shape foil motion. Still, certain limitations apply to these methods, such as that the solid and fluid modes are not correlated or the requirement of the knowledge about the periodic structural behavior. Here we propose a more general method to inspect the modal content of the flow-induced fluttering response of morphing bodies. A conformal mapping technique is used to generate unique energy-based geometrical weights, which enable the modal analysis to be employed for the FSI problems with morphing bodies [41]. The method has no assumption on the geometry and can be applied posterior to the data.

This paper employs the proposed FSI algorithm based on conformal geometry mapping to investigate how an active morphing flap modifies the flow field around a foil. In addition, a reduced-order model of the flap and foil is developed, which, unlike many other reduced order methods, can encapsulate the deforming geometry of the bodies, the nonlinear fluid force feedback, and the flow field created by the motion of the foil. This offers a more refined understanding of the flow-induced fluttering phenomena and can be employed as a fast surrogate model for future

controller designs. We also introduce a multiscale modal analysis technique [42] along with the conformal geometrical weighting [41] to isolate the competing modes in the FSI system. The main contribution of this work can be summarized as (1) developing a high-fidelity body-conformed FSI algorithm to investigate foil and flap system, (2) studying the flow-induced plunging response of a foil with an actively oscillating morphing flap over a wide range of structural parameters, and (3) extending the multiscale proper orthogonal decomposition (mPOD) to FSI system wherein the geometrical weighting is used to explain how the mode competition between the flap-induced and flow-induced modes dictates the fluttering motion of the foil.

The rest of the paper is organized as follows: Section II discusses the fluid-structure interaction method to model a foil with an active flap system and the geometrically weighted mPOD method. In Sec. III we present the results of the system followed by a discussion about the flap-induced and flow-induced flow features in Sec. IV. Finally, in Sec. V we conclude and present potential future directions.

## II. METHODOLOGY

This section will introduce the numerical model and the modal analysis method adopted to investigate the aeroelastic response of an airfoil with an active flap. A two-dimensional energy efficient transport (EET) airfoil immersed in uniform ambient flow is chosen as a model structure. The EET high-lift airfoil [43] was developed by NASA and has been through extensive experimental tests [44] to understand how the multisectional foil design affects the lift generation. It has also been employed for studying the controllable leading and trailing edges to improve the performance of the airfoil using linear models [45,46]. Here we extend these works by incorporating the continuous shape changes of the morphing foil and its flow-induced plunging motions. As shown in Fig. 1(a), the flow-induced fluttering characteristics of the foil are represented with a translational spring-damper system. We focus on the heaving motion of the foil and assume it has a fixed pitching angle. The heaving displacement of the virtual attachment point of the spring system is  $h$ , the geometrical angle of attack (AoA) of the foil relative to the incoming flow is  $\alpha$ , and the angle between the flap and the mean chord line of the foil is  $\theta$ . Comparable models have been used previously to study the flow-induced fluttering response [4,20,47,48]. In the current study, the flap angle  $\theta$  is actively adjusted to represent the morphing flap as the simplest method of the geometrical controller.

### A. Numerical method

The numerical method comprises three main components: setup of the computational mesh, calculation of the dynamic forces, and the fluid-structure interaction procedure, which has been explained in detail and verified in our prior publication [41]. Therefore, we only briefly outline the key components in the following.

A body-fitted grid with a higher resolution near the body is employed to model the highly nonlinear flow around the foil. Here a conformal geometrical mapping technique [49,50] is used to generate a time-variant body-fitted grid. The body contour is segmented in the foil attached coordinate system into points  $z_j = X_j + iY_j$ . The body exterior is then mapped to the exterior of a circle with the radius  $\lambda$ . The cylindrical coordinate along the circle is defined as  $\zeta = \lambda e^{i\phi}$  with  $\phi$  denoting the azimuth angle. The mapping between the two coordinate systems is described with the Laurent series expansion,

$$z(\phi) = \lambda e^{i\phi} + a_0 + \sum_{n=1}^{\infty} a_n e^{-in\phi}, \quad (1)$$

where the coefficients  $a_n$  contain the radial terms  $a_n \equiv \lambda^n b_n$  with  $b_n$  being constant coefficients. We can then obtain the mapping coefficients and optimal coordinates by employing the orthogonality properties of series terms and minimizing the error between the mapped and actual contour points.

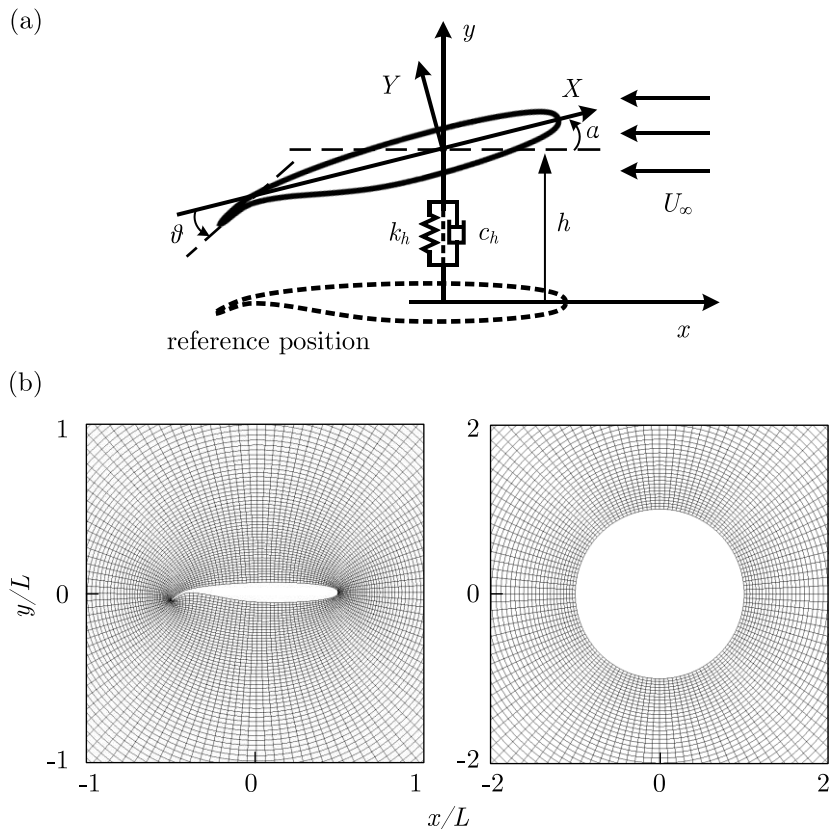


FIG. 1. (a) The cross section of the foil and the model parameters. (b) Sample computational grid around the foil-flap model and the grid mapping to a unit circle.

The grid is constructed in the transformed domain and then mapped to the physical domain with the same set of coefficients acquired from the body contour.

A sample grid generated for the foil with this algorithm is illustrated in Fig. 1(b). The grid is stretched in the radial direction logarithmically to increase its resolution near the surface where large velocity gradients are anticipated. The cylindrical grid in the  $\zeta$  plane is shown in Fig. 1(b). During the simulation, the mesh is updated based on the instantaneous flap angle. The conformal mapping technique also offers a time-invariant grid in the transformed space, allowing the modal analysis techniques. This will be discussed later in Sec. II B.

The flow field is modeled with a modified Navier-Stokes equation based on the vorticity-stream function ( $\omega - \psi$ ) formulation in the transformed domain. An implicit, second-order finite difference approach proposed by Guglielmini *et al.* [47] and Zhu *et al.* [20] is used to solve the following system of equations:

$$\frac{\partial \omega}{\partial t} + \frac{1}{\sqrt{J}} \left[ v_r \frac{\partial \omega}{\partial r} + \frac{v_\phi}{r} \frac{\partial \omega}{\partial \phi} \right] = \frac{1}{\text{Re} J} \left[ \frac{\partial^2 \omega}{\partial r^2} + \frac{1}{r} \frac{\partial \omega}{\partial r} + \frac{1}{r^2} \frac{\partial^2 \omega}{\partial \phi^2} \right], \quad (2)$$

$$\frac{\partial^2 \psi}{\partial r^2} + \frac{1}{r} \frac{\partial \psi}{\partial r} + \frac{1}{r^2} \frac{\partial^2 \psi}{\partial \phi^2} = -J\omega, \quad (3)$$

where  $\text{Re}$  is the Reynolds number and  $J$  is the temporally and spatially varying determinant of the Jacobian of  $\zeta = \xi + i\eta \Rightarrow z = X + iY$  transformation. The radial and azimuthal flow velocities,  $v_r$  and  $v_\phi$ , respectively, include the time-dependent effect of the transformation. The no-slip boundary

condition is applied on the foil surface and uniform flow condition with  $\vec{v} = [U_\infty, 0]^T$ , and  $\omega = 0$  is applied at the far-field boundaries.

After the vorticity and stream function are solved in the transformed domain, the inverse mapping transformation is used to calculate flow data in the physical domain. The nondimensionalized pressure, hydrodynamic force, and hydrodynamic moment exerted on the foil are then calculated using the following equations, integrated along the foil boundary in the transformed domain:

$$p(\phi) = p_0 + \int_0^\phi \left( \frac{\partial p}{\partial X} \frac{\partial X}{\partial \phi} + \frac{\partial p}{\partial Y} \frac{\partial Y}{\partial \phi} \right) d\phi, \quad (4)$$

$$\frac{F_X}{\rho U_\infty^2 L} = \int_0^{2\pi} -p \frac{\partial Y}{\partial \phi} + \frac{2}{\text{Re}} \left[ \frac{\partial Y}{\partial \phi} \frac{\partial U}{\partial X} - \frac{1}{2} \frac{\partial X}{\partial \phi} \left( \frac{\partial U}{\partial Y} + \frac{\partial V}{\partial X} \right) \right] d\phi, \quad (5)$$

$$\frac{F_Y}{\rho U_\infty^2 L} = \int_0^{2\pi} p \frac{\partial X}{\partial \phi} + \frac{2}{\text{Re}} \left[ \frac{1}{2} \frac{\partial Y}{\partial \phi} \left( \frac{\partial U}{\partial Y} + \frac{\partial V}{\partial X} \right) - \frac{\partial X}{\partial \phi} \frac{\partial V}{\partial Y} \right] d\phi, \quad (6)$$

where  $U$  and  $V$  are the nondimensional flow velocity components in the  $X$  and  $Y$  directions in the body attached coordinate system.

The structural heaving velocity,  $\dot{h}$ , is updated, through a tightly coupled algorithm, using the calculated forces  $F$  in the vertical direction:

$$m_f \ddot{h} + c_h \dot{h} + k_h h = F, \quad (7)$$

where  $m_f$  is the mass of the foil, and  $c_h$  and  $k_h$  are the damping and stiffness coefficients for heaving motions, respectively. The vibration from the change of center of the mass when the flap moves is ignored in the current study as its contribution is negligible with small flap mass and movement. However, for applications with larger deformation or when the flap occupies significant body weight, this should be taken into account.

The fluid equations are discretized in  $r$ ,  $\phi$ , and  $t$  and solved in the transformed domain. A second-order central difference scheme is employed for the vorticity transport equation. The vorticity field is updated at each time step via the alternative direction implicit technique [51]. The Poisson equation is solved with a semispectral method, wherein the Fourier transformation is employed along the azimuthal direction, and the second-order finite-difference method is used along the radial direction.

The proposed procedure can successfully capture the nonlinear interaction between the fluid and structure. The model has been validated with several canonical problems in the authors' previous publication [41]. In Appendix A we present the grid refinement study for the current research.

## B. Geometrically weighted multiscale proper orthogonal decomposition

The FSI response of the foil and flap system involves different timescales, including the flap oscillation, the plunging foil, and the vortex shedding. To analyze this system and compare different mechanisms, we use the multiscale POD [42] with geometrical weighting [41,52]. This section will summarize the main components of the method.

Geometrically weighted modal analysis (GW-MD) obtains weighting functions through the Jacobian of the conformal mapping, which combines the structural motion and flow structure into a single spatiotemporal basis. GW-MD permits the use of data-driven modal analysis methods for FSI systems with deforming bodies. The procedure conserves the modal energy content and reveals how the structure and flow interact. To identify dominant flow modes for active flap cases, GW-MD is further extended to allow multiscale modal calculation. In particular, multiscale POD (mPOD) is applied in which a filter bank enables the splitting of the frequency spectrum into different scales. The frequency spectrum is preserved within each scale, and the corresponding optimal orthogonal eigenbases are assembled into a single mPOD basis. The following steps are done to perform geometrically weighted multiscale POD (GW-mPOD):

(1) Selecting the flow data: in this study, we use vorticity to realize how the coherent structures form and dissipate. The  $n$  snapshots of dimension  $n_r \times n_s$  are rearranged into column vectors of  $\mathbf{u} \in \mathbb{R}^{n_r n_s \times 1}$  and assembled to form the data matrix  $\mathbf{U} \in \mathbb{R}^{n_r n_s \times n}$ .

(2) Computing the correlation matrix: the correlation matrix is calculated using  $\mathbf{C} = (\mathbf{J} \odot \mathbf{U})^+ (\mathbf{J} \odot \mathbf{U})$  wherein the Jacobian is used as the weighting function ( $\mathbf{J} \in \mathbb{R}^{n_r n_s \times n}$ ). Here  $\odot$  denotes Hadamard product defined as  $(A \odot B)_{ij} = A_{ij} B_{ij}$  with  $i$  and  $j$  being free indices.

(3) Construction of the filter bank: the filter bank is formed to contain  $m$  filters,  $\mathbf{H}_1, \dots, \mathbf{H}_m$ . It is used to split  $\mathbf{C}$  into  $m$  nonoverlapping contributions. The filter bank, in this research, is determined from the discrete Fourier transform of the correlation matrix. The filter bank consists of a low-pass filter, a high-pass filter, and a series of band-pass filters. The cutoff frequency of each band-pass filter is selected so that each filter contains an isolated spectral peak of the correlation matrix. The filter bank spans the entire spectrum, so the spectral content of the data set is retained through the partition. The data matrix is filtered in the spectral domain and transformed back to the temporal domain. POD is then performed on each temporal partition. An example process of applying a filter bank will be shown in Sec. IV, and readers are referred to the pioneering paper [42] for mathematical details.

(4) Decomposing the correlation data matrix: Using the  $m$  filters, the correlation matrix can be decomposed as  $\mathbf{C} \approx \sum_{i=1}^m \Psi_i \sigma_i^2 \Psi_i^T$ , where  $\Psi$  is the temporal structure. Moreover, with the enforcement of the orthogonality condition, the spatial structures can be written as  $\Phi = \mathbf{U} \Psi \sigma^{-1}$ . The spatial structures  $\Phi$  are sorted in descending order based on their contribution to the energy content.

GW-mPOD has several unique benefits over alternative modal analysis methods for the current study. POD modes often suffer from spectral mixing. While DMD can produce modes with a single frequency for each, those modes are not energetically relevant and not orthogonal. mPOD finds coherent structures with similar energy contents to POD modes, but at the same time, it reduces the spectral mixing problem. When combined with the geometrical weighting method, the analysis can identify coherent flow structures related to the structure motion and internal flow dynamics. The identified flow features can then be compared based on their contribution to the energy content. The results will be demonstrated in Sec. IV.

### C. Problem setup and summary

The parameter space of the FSI system in the current study includes the structural parameters, fluid properties, and active flap parameters. We focus primarily on how the active actuation of the flap affects the flow-induced plunging response of the foil. Sinusoidal oscillatory motions with different frequencies and amplitudes are imposed on the flap with a particular average angular position. Simulation parameters are defined as follows:

(1) *Flow parameters*: The computational domain is extended to  $15L$  around the foil and flap system, with  $L$  being the chord length of the foil. A grid with a resolution of  $(280 \times 256)$  in radial and angular directions, respectively, is applied to the fluid domain. The ambient flow velocity  $U_\infty$  is chosen as the characteristic velocity scale, and the foil chord length  $L$  is used as the length scale. Following previous literature [47,53], the Reynolds number based on the chord length is fixed at  $\text{Re} = \frac{U_\infty L}{\nu} = 1000$ . This Reynolds number is sufficiently large to allow the complex vortex shedding that drives the fluttering phenomenon.

(2) *Physical parameters of the foil*: The mass ratio of the foil is set to  $m \equiv \frac{m_f}{\rho L^2} = 0.1$ . The rotational degree of freedom of the foil is fixed and only the heaving motion is permitted. The spring-damper system is considered with the nondimensional stiffness of  $\frac{k_h}{\rho U_\infty^2} = 1.0$  and Rayleigh stiffness proportional damping of  $c_h = \lambda_c k_h$  with  $\lambda_c = 0.1 \frac{U_\infty}{L}$ . The flap length  $l$  is selected based on the NASA design [43] as  $0.12L$ . The roles of structural stiffness and damping on the flow-induced motion are discussed in Appendix B.

(3) *Control parameters of the active flap*: A periodic pitching motion is imposed on the flap as  $\theta = \theta_0 + A \sin(\Omega t)$ , where  $\theta_0$  and  $A$  are the mean angle and the amplitude of the flap relative to the

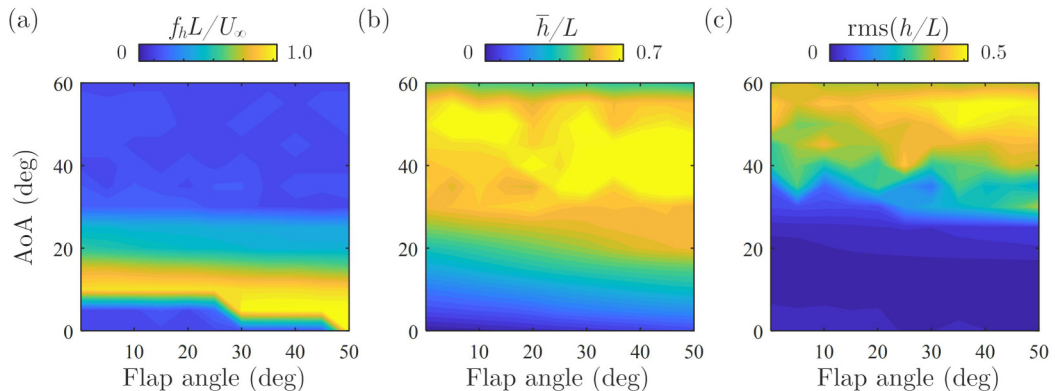


FIG. 2. (a) Dominant frequency of the heaving motion, (b) mean heaving displacement, and (c) rms of heaving amplitude of the uncontrolled cases.

chord, respectively, and  $f = \frac{\Omega}{2\pi}$  is the frequency of the flap oscillation. In the rest of this paper, we use the flap's Strouhal number,  $St_f = \frac{fL}{U_\infty}$ , to refer to the actuation frequency.

### III. FLOW-INDUCED RESPONSE OF A FOIL WITH AN ACTIVE FLAP

The plunging response of a heaving foil subject to ambient flow and forced morphing flap motion is discussed in this section. Representative cases are inspected to identify the reasons behind different dynamic responses. The Fourier transform is employed to find the characteristic frequencies of the heaving motion. We identify how the motion evolves and how the trajectory of the foil motion changes in each period with the help of the phase portrait plot, a mapping between the heaving displacement  $h$  and heaving velocity  $dh/dt$ . In addition to the structural response, the coherent structures associated with the dominant frequencies are examined with GW-mPOD. We will primarily consider a small angle of attack of  $\text{AoA} \leq 10^\circ$  as this is within common operating conditions.

As a baseline, we consider the uncontrolled case where the flap is fixed at a specified AoA. Figure 2(a) shows the dominant heaving frequency of the uncontrolled cases. The dominant frequency is highly dependent on the AoA. At low AoA, the flow is attached, and the airfoil has a minimal mean displacement and oscillation amplitude as shown in Figs. 2(b) and 2(c). When the flow is attached, the heaving added mass coefficient for a NACA0012 airfoil is  $a_{22} \sim 0.79$  [54] as we fixed the movement to only vertical plunging. The analytical natural frequency can be approximated as  $f_0 = \frac{1}{2\pi} \sqrt{\frac{k}{m_f + m_a}} \sim 0.19$ , where  $k = 1.0$  is the nondimensional stiffness and the total virtual mass  $m$  combining foil mass  $m_f$  and added mass  $m_a$  is  $m = m_f + m_a = 0.1 + a_{22}\pi\rho 0.5^2 \sim 0.72$ . The calculated natural frequency is very similar to what we observed in Fig. 2(a) where the heaving frequency falls in the range of 0.16 when the flow remains attached with  $\text{AoA} = 0$ . In the moderate AoA range, the continuous vortex shedding induces vortex-induced vibration, still with a small amplitude. In these cases, a narrow-band frequency response appears due to the alternative vortex shedding from the leading and trailing airfoil edges. The vortex shedding forms a regular vortex street in the wake and induces a steady periodic heaving motion. Interestingly, for the flap angles higher than a certain threshold, the apparent foil shape is modified and the periodic vortex shedding shifts to higher AoA. This response switch occurs at an average flap angle of  $\theta \sim 30^\circ$ . Large mean heaving displacement and oscillation amplitude are observed at higher AoAs due to the nonperiodic vortex shedding from the leading and trailing edges and the airfoil stall at  $\text{AoA} \sim 50^\circ$ . The flap angle is not a decisive factor in this regime. Instead, the vortex-induced vibration is primarily affected by the AoA.

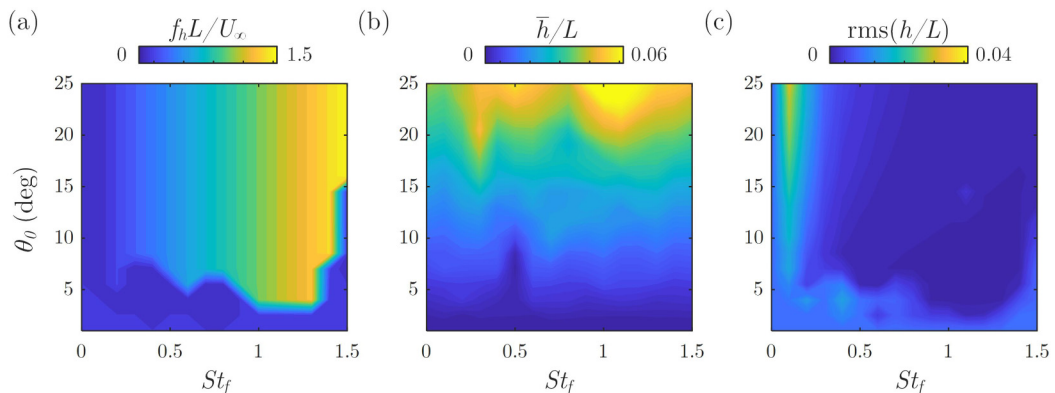


FIG. 3. (a) Dominant nondimensional heaving frequency, (b) mean heaving displacement, and (c) unsteady heaving amplitude (rms) for AoA = 0° and different flap positions  $\theta_0$  and flap frequency  $St_f$ . Flap amplitude is fixed at  $A/\theta_0 = 1$ .

Figure 3 shows how the foil heaving frequency  $f_h$ , average heaving displacement  $\bar{h}/L$ , and unsteady heaving motion of the foil vary with mean flap angle and flap frequency when the foil is at AoA = 0°. Here it is assumed that  $A/\theta_0 = 1$ . When the amplitude is small, the flap motion does not lead to the plunging motion of the foil. At larger amplitudes, on the other hand, the foil starts to vibrate at the exact flap frequency. No significant change in vortex shedding pattern is observed even at larger flap amplitudes, and the heaving displacement remains very small. From the uncontrolled case, we can extract the average heaving displacement at AoA = 0° and compare the difference between flap angle  $\theta = 0^\circ$  and  $\theta = A$ . It is seen that this value matches with the heaving amplitude in the active flap case with flap frequency  $St_f = 0.1$ . This implies that when the flap is moving slowly, the change of the lift coefficient determines the heaving motion. However, when the flap frequency increases, we see a small heaving amplitude indicating almost no vibration. What happens is that the flap moves too fast and the induced motion from the change of lift is damped out. The cause of the small heaving motion at a higher flap frequency, with the same frequency as the flap motion, is the added mass effect due to the flap motion.

An increase in AoA prompts substantial changes. Figure 4 plots the heaving response with AoA = 10° and a small flap amplitude of  $A = 1.5^\circ$ . At low flap frequencies, the foil heaves at

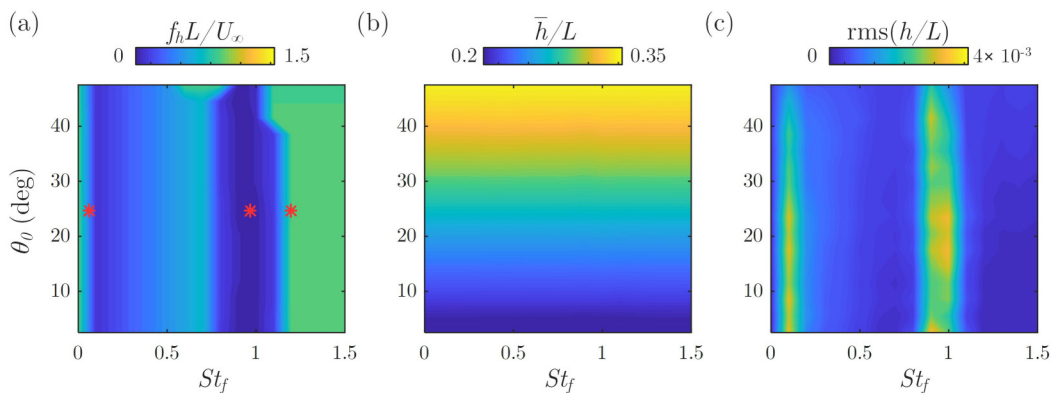


FIG. 4. (a) Dominant nondimensional heaving frequency, (b) average heaving displacement, and (c) heaving amplitude (rms) for AoA = 10° with flap amplitude  $A = 1.5^\circ$  at different average angle  $\theta_0$ .



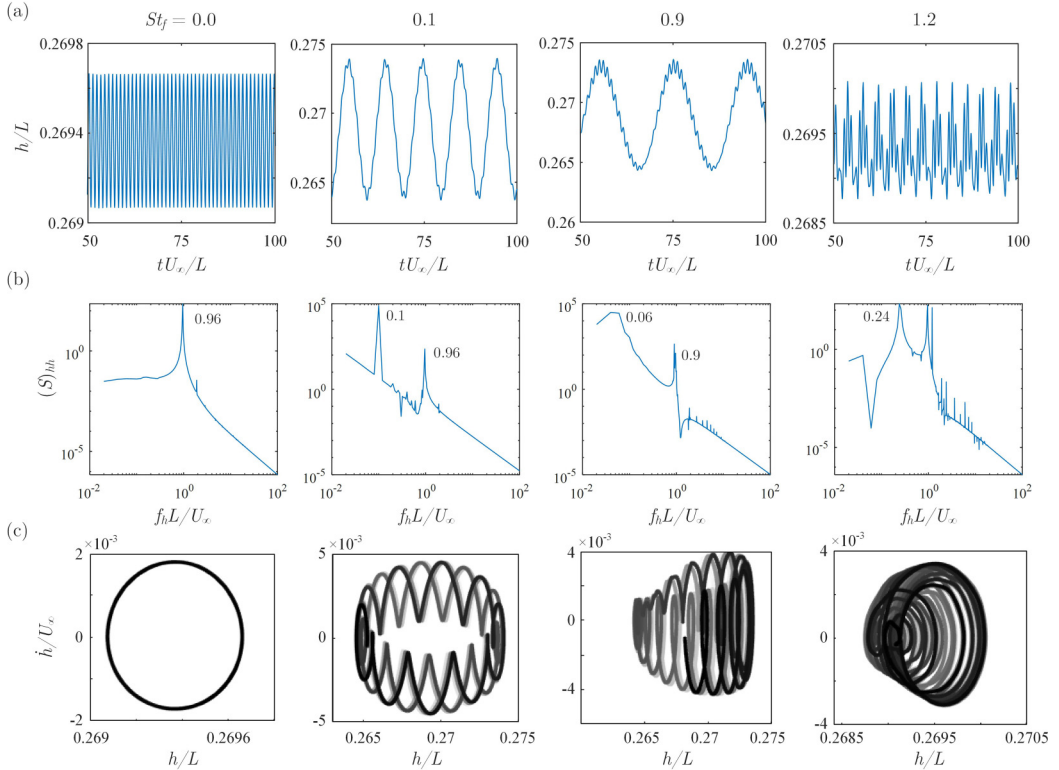


FIG. 5. The (a) heaving motion time histories, (b) power spectra, and (c) the phase portraits of  $St_f = 0.0, 0.1, 0.9, 1.2$ . It is assumed that  $AoA = 10^\circ$ ,  $\theta_0 = 24^\circ$ , and  $A = 1.5^\circ$ .

the flap frequency, while at higher flap frequencies, the foil switches its dynamic response and instead oscillates at a terminal fixed frequency. Interestingly, a low-frequency band around the natural vortex-induced heaving frequency ( $f_h L/U_\infty \sim 0.96$ ) separates these two dynamic regions. The amplitude plot shows that this low-frequency band coincides with the large vibration amplitude. We will take a deeper look at this region later. Also, similar to the zero AoA case, a narrow large heaving amplitude band is located at  $St_f \sim 0.1$ . This amplitude is similar to the difference of the heaving displacement with different static flap angles (uncontrolled cases). The slow flap movement changes the lift coefficient, which causes a large-amplitude vibration. This effect is damped out at higher flap frequencies, but the flap-induced vortex street creates another large-amplitude peak, as will be explained. The mean heaving displacement is only proportional to the mean flap angle, whereas the larger mean flap deflection results in a higher lift force on the foil and larger mean displacement.

To further explain the characteristic dynamics of these two regions, three representative cases are discussed below. All of these three active flap cases have the same AoA of  $10^\circ$ , flap average position  $\theta_0 = 24^\circ$ , and flap amplitude  $A = 1.5^\circ$ , but with different flap frequencies of  $St_f = \{0.1, 0.9, 1.2\}$ . The selected cases are also marked in Fig. 4(a). Figure 5 shows the heaving displacement over a certain time interval, the power spectrum of the heaving displacement calculated from 10 flapping cycles, and the phase portrait of these cases. The phase portrait trajectories are marked with white to black based on its temporal state. The uncontrolled case  $St_f = 0.0$  is also included for cross-comparison.

The uncontrolled case with no flap motion undergoes a periodic oscillation with a frequency of 0.96 due to the vortex-induced vibration. This response mode is referred to as the flow-induced mode

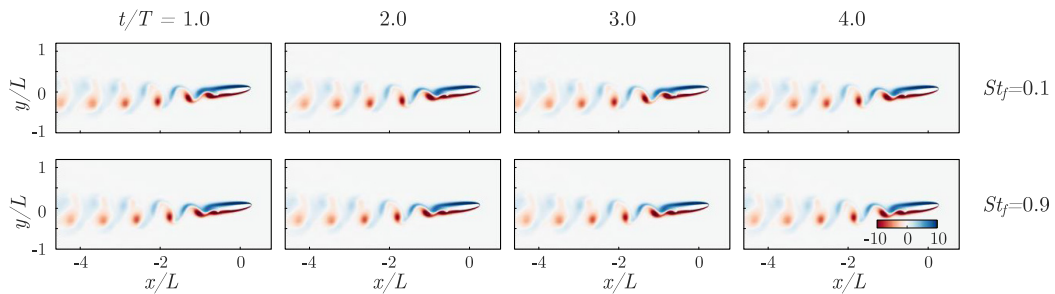


FIG. 6. Instantaneous vorticity fields over four active flap periods of  $St_f = 0.1$  and  $St_f = 0.9$ .  $T$  is the flap motion period.

from now on. When the actuation is activated, we can see that torus-like trajectories emerge for all three selected cases. The heaving time history involves large-scale oscillation and small-amplitude unsteady fluctuation. Furthermore, the spectrum clearly shows multiple distinct peaks indicating that the system is quasiperiodic, and the observed dynamics are from mode competition between different mechanisms. In particular, the  $St_f = 0.1$  case has distinct peaks at the flap frequency 0.1 and flow-induced frequency 0.96, while the other case with  $St_f = 0.9$  shows two peaks at the frequencies of 0.9 and 0.06. Although they share a very similar heaving response and flow field (shown in Fig. 6), in a previous study [41] we highlighted that other mechanisms are involved in these two cases. The results will be confirmed in Sec. IV using the GW-mPOD analysis with extra knowledge of the energy content and the competition between the modes. In the low flap frequencies, the flap motion does not substantially modify the downstream wake and mainly adjusts the exit angle of the vortex wake. On the other hand, the flap motion of  $St_f = 0.9$  creates a wake structure that interferes with the flow-induced mode. The other case of  $St_f = 1.2$  exhibits a much smaller heaving amplitude similar to the nonactuated case and delivers a larger heaving movement closer to quasiperiodic motion.

A very different foil-fluid interaction response is observed for the flap with a large oscillation amplitude of  $A = \theta_0$  (Fig. 7). Here the low-frequency band narrows, while the foil still undergoes a substantial heaving motion at the flap frequency outside of this band. Interestingly, two branches of the low-frequency band are observed. Furthermore, the average heaving displacement does not increase monotonically with the average flap angle when the flap amplitude is small. Instead, it displays a unique peak near the natural frequency range. The heaving amplitude peak at the slow

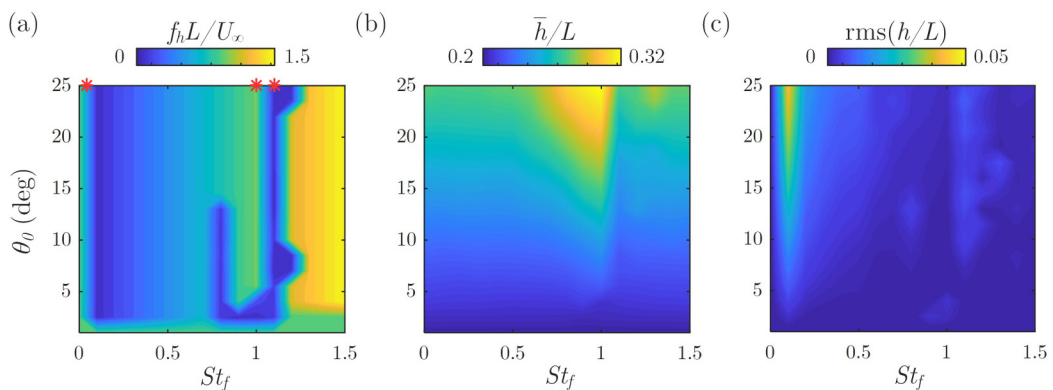


FIG. 7. (a) Dominant nondimensional heaving frequency, (b) mean heaving displacement, and (c) unsteady heaving amplitude (rms) for  $AoA = 10^\circ$  with the large-amplitude flap motion of  $A/\theta_0 = 0$ .

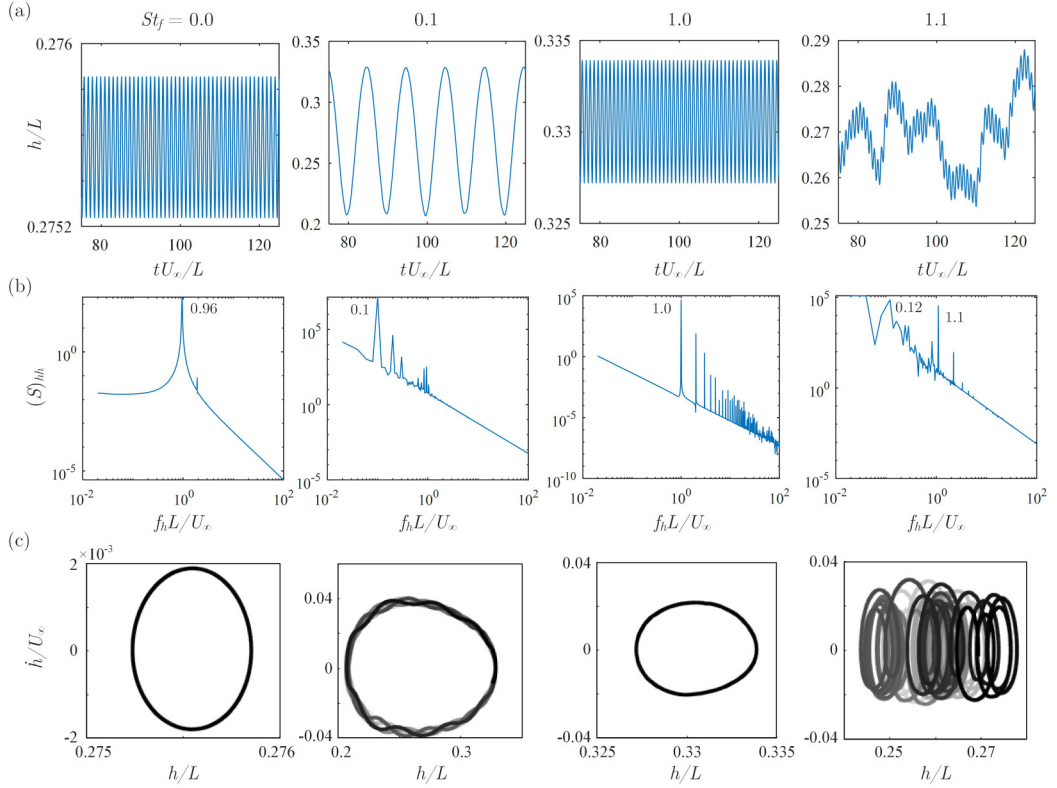


FIG. 8. The heaving displacement time history, power spectrum, and phase portrait plot of  $St_f = 0.0, 0.1, 1.0, 1.1$ , respectively, from the top to bottom row. The results are for  $AoA = 10^\circ$  and  $A = \theta_0 = 24^\circ$ .

flap frequency emerges again for the same reason as before: the slow transition of the overall lift coefficient.

The time history, power spectrum, and phase portrait of the heaving motion are shown in Fig. 8. Rows are associated with different flap actuation frequencies of  $St_f = \{0, 0.1, 1.0, 1.1\}$ . When  $St_f = 0.1$ , the larger flap oscillation amplitude creates a stronger pressure gradient over the flap. During the downsweep flap motion, the pressure gradient creates a new vortex behind the trailing edge. The newly formed vortical structure then separates from the flap during the upsweep phase and merges into the wake. The leading-edge vortex shedding is locked onto the same period due to the large suction pressure caused by the flap, which results in the purely periodic motion at the flap frequency  $St_f = 1.0$ . This can be identified from the clear resonance peaks in the power spectrum and periodic orbit in the phase portrait. A similar lock-in phenomenon has been reported in several recent studies of airfoils with morphing surfaces [55–57].

When the flap frequency increases to  $St_f = 1.1$ , the vortex shedding from the trailing edge becomes chaotic (Fig. 9). The leading-edge vortex shedding mode is controlled by the foil geometry, while at the trailing edge, the flow separation is dictated by the flap motion. Since there is a discrepancy between the flap frequency and natural vortex shedding frequency at the trailing edge, an intermittent wake structure is formed. The heaving motion is consequently chaotic, as demonstrated by the never-repeating trajectory in the phase portrait.

The large heaving amplitude of  $St_f = 0.1$  originates from the low-frequency and large-amplitude lift forces changes driven by the continual geometrical changes. When the flap slowly varies its angle, it modifies the lift force at different vibration stages. Consequently, the fluid-structure

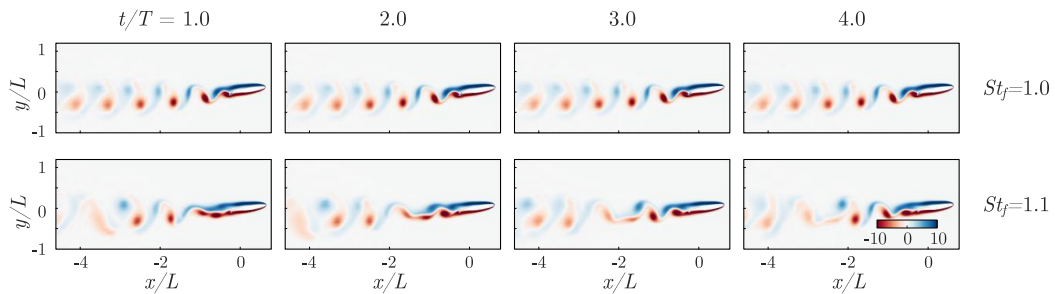


FIG. 9. Instantaneous vorticity field over four active flap periods of (a)  $St_f = 1.0$  and (b)  $St_f = 1.1$  with  $AoA = 10^\circ$  and flap motion  $A = \theta_0 = 24^\circ$ .

interaction of the foil is quasistatic, where the flap movement does not create a new vortical structure, but it still affects the foil heaving motion by modifying the instantaneous lift force. This is supported by the presence of a spectrum peak at flap frequency  $fL/U_\infty = 0.1$ . This peak is present in all three cases discussed so far, and the mechanism behind it can be related to the uncontrolled benchmark cases.

In summary, the flap oscillating with a larger amplitude impacts the flow and heaving motion more than the smaller amplitude cases. The larger flap amplitude substantially modifies the flow at the flap location and plays a controlling role in determining system response compared to the smaller amplitude cases. When the flap frequency approaches the natural frequency, there is a lock-in condition, and the foil heaves at the same frequency as the flap movement. On the other hand, when the flap frequency increases further, there is substantial vortex shedding from the flap and foil surfaces resulting in a chaotic heaving motion of the foil. Finally, at a specific low frequency, the slowly changing geometry leads to quasistatic relocation of the foil through a readjustment of the flow. After observing such a diverse interaction between the flap-induced and flow-induced modes, a question arises: is there an index that can classify the competition between these two characteristic modes and represent the system behavior? This is achieved using the GW-mPOD analysis in the next section.

#### IV. MODE COMPETITION BETWEEN FLAP-INDUCED AND FLOW-INDUCED MODES

We now apply the GW-mPOD analysis to the observed vorticity field and investigate the interaction between different fluid dynamic modes that drive the foil's heaving motion. More than 30 flap oscillation cycles with at least 10 snapshots per cycle are used to perform the modal analysis for all the following cases.

Figure 10 demonstrates the GW-mPOD procedure for the foil-flap case of  $AoA = 10^\circ$  and  $St_f = 0.1$ . Here flap actuation is fixed at  $A = 1.5^\circ$  and  $\theta_0 = 24^\circ$ . Figure 10(a) shows the discrete Fourier transform of the geometrically weighted temporal correlation matrix, and based on the intensity (spectral power), the correlation matrix is partitioned with the filter bank as shown in Fig. 10(b). A conventional snapshot POD procedure [58] is then applied to each partition. The flow vorticity modes are sorted based on their enstrophy contribution. All the leading modes contain pure spectral contents and are associated with different dynamic responses.

The GW-mPOD is employed for representative cases identified in the previous section. The first case is with a small-amplitude flap motion and  $St_f = 0.1$  [Fig. 10(c)]. Here mode 2 has the same pattern and frequency as the uncontrolled case; thereby, it is called the flow-induced mode. On the other hand, mode 4 has the same frequency as the flap oscillation and is denoted as the flap-induced mode. We can see that there is little extended wake in this mode, so it affects only the area close to the trailing edge. The trailing edge vorticity field shows two nonconvective vortical structures formed through the slow flap sweeping motion. The slower motion does not create enough

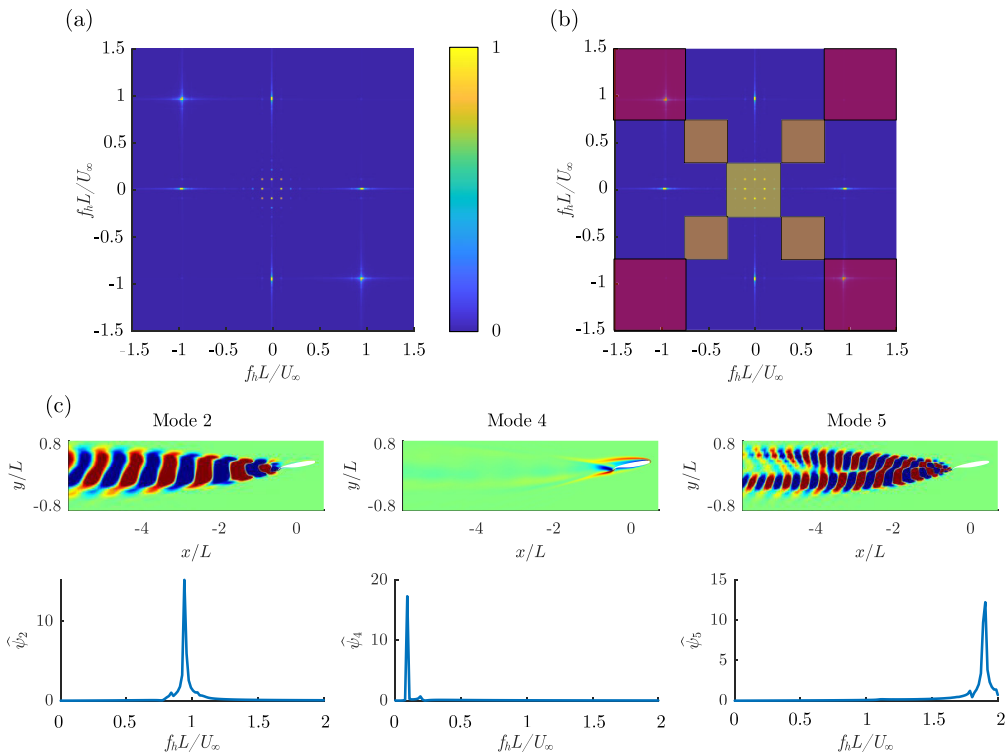


FIG. 10. (a) The discrete Fourier transform (DFT) of the normalized temporal correlation matrix; (b) partitioned correlation matrix. (c) The spatial structure and spectrum of the leading modes of the case  $\text{AoA} = 10^\circ$  with flap frequency  $\text{St}_f = 0.1$ , amplitude  $A = 1.5^\circ$ , and average angle at  $\theta_0 = 24^\circ$ . The modes are normalized based on their respective largest vorticity, which is the same for the following figures.

pressure change to force vortex shedding but can adjust the exit angle of the flow-induced wake at the trailing edge. This is why the foil undergoes quasiperiodic motion, with two distinctive modes superimpose upon each other. The slow modulation of the flap changes the direction of the steady vortex shedding, modifies the lift force, and results in a low-frequency, high-amplitude heaving motion.

Similar behavior can be observed for other flap frequencies with  $\text{St}_f \leq 0.8$  [Figs. 11(a) and 11(b)]. However, when the flap frequency reaches  $\text{St}_f = 0.9$  [Fig. 11(c)], the flap-induced vortices propagate into the wake. At higher frequencies, the flap-induced mode has a clear extended wake as demonstrated for  $\text{St}_f = 1.2$  [Fig. 11(d)]. There will be subsequent interference between the flap-induced and flow-induced modes when the flapping frequency increases. Here a stronger pressure gradient from the flap motion induces a new convective wake structure, and, consequently, the interference between two energetically similar wakes promotes quasiperiodic motion of the foil.

The large flap oscillation amplitude of  $A = \theta_0 = 24^\circ$  is considered next. Figure 12 shows the leading flap-induced and flow-induced modes along with the frequency spectrum of the representative cases. We observed that  $\text{St}_f = 0.1$  [Fig. 12(a)] exhibits large-amplitude, low-frequency plunging motion similar to the case with small flap amplitude. The flap-induced mode also shows a comparable spatial pattern, indicating that both cases are alike at modifying the exit angle of the trailing edge wake. However, the vorticity intensity is much stronger here, and the flap-induced mode contributes more to the enstrophy than the flow-induced mode. Once the flap frequency increases beyond  $\text{St}_f = 0.3$ , an extended wake develops. At the higher flap frequency of  $\text{St}_f = 0.8$  [Fig. 12(c)], the flap-induced and flow-induced modes share the same frequency, and the system

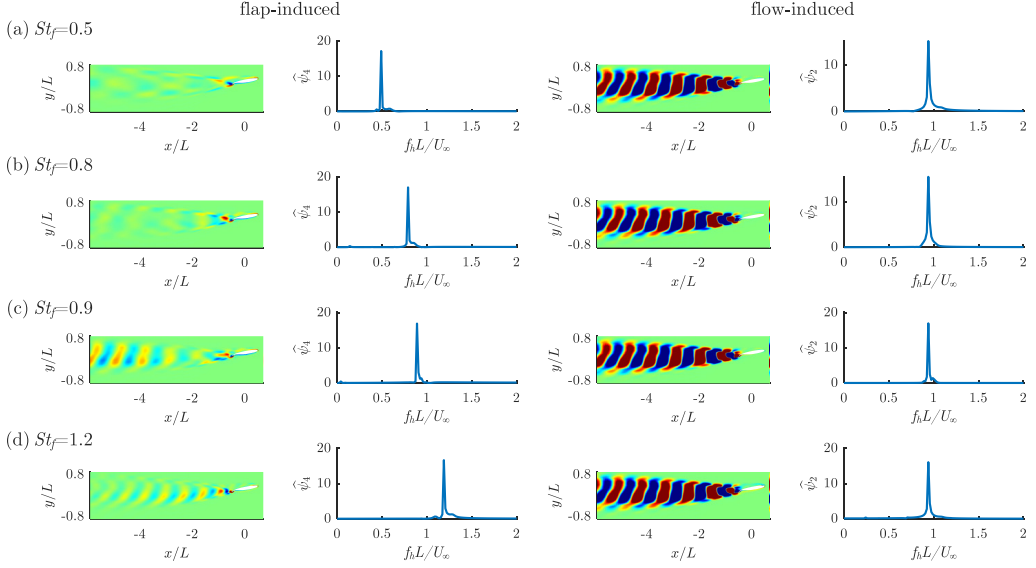


FIG. 11. The spatial structures and spectra of the leading flap-induced and flow-induced modes of the case  $\text{AoA} = 10^\circ$  with flap amplitude  $A = 1.5^\circ$ , average angle  $\theta_0 = 24^\circ$ , and different flap frequency  $St_f$ .

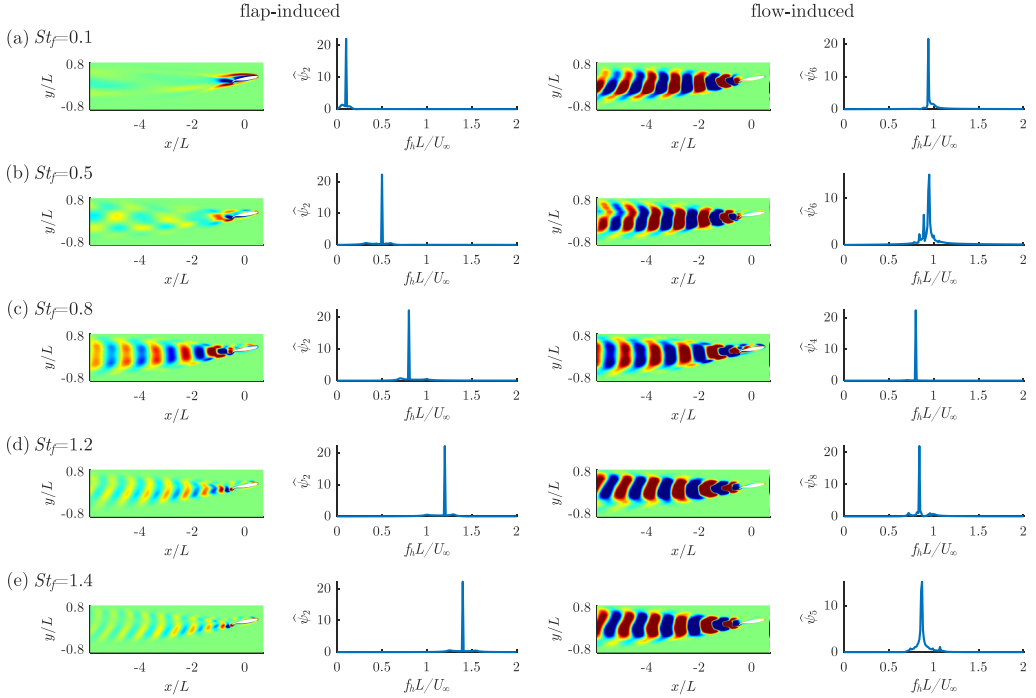


FIG. 12. The spatial structures and spectra of the flap-induced and flow-induced modes of the case  $\text{AoA} = 10^\circ$  with flap amplitude  $A = \theta_0 = 24^\circ$  and different flap frequency  $St_f$ . The modes are normalized based on their respective largest vorticity.

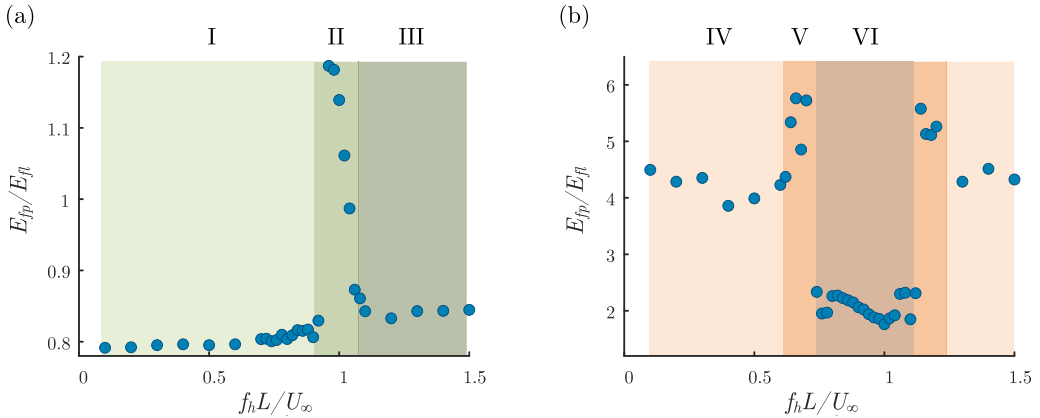


FIG. 13. Ratio of the leading flap-induced and flow-induced modal energy of AoA = 10° case with (a) small flap amplitude  $A = 1.5^\circ$  and average angle  $\theta_0 = 24^\circ$  and (b) large amplitude  $A = \theta_0 = 24^\circ$ . See text for explanation of the Roman numbers.

is in a perfect lock-in state. This is different from the small-amplitude case where the flow pattern is similar, but the frequencies of these modes are different. By increasing the flap frequency to  $St_f = 1.2$  [Fig. 12(d)], the flap- and flow-induced modes separate again.

We calculated the modal enstrophy ratio between the leading flap-induced ( $E_{fp}$ ) and flow-induced ( $E_{fl}$ ) modes for the small and large flapping amplitude and different flapping frequencies (Fig. 13). In both cases, the enstrophy ratio can be divided into three regions. First, we consider the small-amplitude case in Fig. 13(a). At low flap frequencies,  $E_{fp}/E_{fl} \sim 0.8$ , but it suddenly jumps to much larger values of  $E_{fp}/E_{fl} \sim 1.2$  when flap oscillation approaches the flow-induced vibration frequency. The enstrophy ratio eventually drops gradually after  $St_f > 1$  to  $E_{fp}/E_{fl} \sim 0.85$ . At a much higher  $St_f$  range, the ratio increases with a much milder slope. Although the plunging motion could be classified as quasiperiodic with multiple distinct peaks in all cases, the three regions indicate three different physical mechanisms, denoted with Roman numbers in Fig. 13. When the flap oscillation amplitude and frequency are both small (I), the flap-induced mode is limited to adjusting the exit angle of the flow-induced wake. At large flap frequency (III), the flap motion induces extended wake, which has higher enstrophy and interferes with the flow-induced wake. Finally, when the flap frequency approaches the flow-induced frequency (II), the two modes have comparable enstrophy and similar spatial structure, which indicates the lock-in phenomenon where the flow-induced mode transports enstrophy to the flap-induced mode and hence are correlated. Recall that in Fig. 4(a) we also saw three different regions in the heaving frequency, and the reason behind that is now clear: the flow-induced and flap-induced modes each have a different controlling role at different flap frequencies.

The enstrophy ratio of the large-amplitude case shown in Fig. 13(b) reveals a different story compared to the small-amplitude case. Now the flap-induced mode is always more energetic than the flow-induced mode. Again, three distinct regions can be identified. The first region is associated with a large dissimilarity of the flap-induced and flow-induced modal frequencies and  $E_{fp}/E_{fl} \sim 4$  (IV). In this region, the flap-induced and flow-induced modes coexist, leading to quasiperiodic motion. When the frequencies become closer, the enstrophy ratio increases to  $E_{fp}/E_{fl} > 5$  (V), implying that the flap-induced mode overpowers the flow-induced mode. The flap-induced vortex shedding dominates the flow, but the slightly mismatched leading-edge vortex shedding results in an unsteady lift force that eventually destabilizes the heaving motion. This explains why there are two branches of low-frequency bands in Fig. 7(a): the flap-induced mode is dominant, and the flow-induced mode is not locked in due to the larger frequency gap between them, leading to a chaotic foil heaving behavior. Within the lock-in region we see that the enstrophy ratio drops to  $E_{fp}/E_{fl} \sim 2$  (VI). Once

locked in, the leading edge vortex shedding is now guided by the trailing edge flap motion, and the two modes excite the same flow modes. In both small- and large-amplitude cases, we observe that the energy is transported from the more energetic to less energetic mode. Hence, the enstrophy ratio is closer to unity. Due to the more energetic flap-induced mode, the lock-in region is wider for larger flap amplitude cases.

We now summarize the findings from the GW-mPOD analysis. There are two competing modes: flap-induced and flow-induced modes. When the flap oscillation amplitude is small, the two modes have a similar energy level and coexist to create quasiperiodic heaving motion. When the flap frequency is small, the flap quasistatically modifies the exit angles of the flow-induced wake, while at higher flap frequencies, the flap induces an extended wake that interferes with the flow-induced mode. On the other hand, when the flap oscillation amplitude is large, the flap-induced mode contains considerably higher energy and is the dominant mechanism. Mainly, when the frequencies of the two modes approach each other, a strong lock-in effect is observed. The trailing edge motion guides the leading edge vortex shedding, and the two competing modes share a similar energy content. The observations can also explain why, in the smaller flap amplitude cases, the flow fields look similar throughout different actuation (Fig. 6), but in the larger flap amplitude cases, flow changes significantly (Fig. 9). Basically, in the larger flap amplitude case, the flap-induced modes have higher enstrophy and can strongly interfere with the flow-induced modes. GW-mPOD successfully reveals how these two passive and active modes bring rich dynamics to the system. The modal enstrophy ratio between these modes is identified as a predictive indicator of the nature of plunging motion.

## V. CONCLUSION

In this paper, we employed a strongly coupled FSI algorithm to study the flow around a deforming geometry. Different analysis methods, including a geometrically weighted multiscale modal analysis technique, are adopted to dissect the flow field. We explored dominant dynamic interaction modes that could be useful for designing control strategies to regulate the flow-induced fluttering response. Deployment of the GW-mPOD method leads to valuable observations of this complex FSI system, summarized as follows: (1) when the flap amplitude and AoA of the foil are small, the flap and flow-induced modes are equally important and the interaction between them primarily creates quasiperiodic motion; (2) at larger flap amplitudes, the flap-induced vortex shedding dominates the foil heaving motion, causing the heaving motion to lock onto the flap oscillation frequency; (3) the ratio of the flap-induced and flow-induced GW-mPOD modal energy is a discriminative indicator of the flow field and flow-induced vibration of the system. For the AoA considered, the active control surface is an effective mechanism in modulating the flow and regulating the foil motion.

The proposed methodology utilizes multiscale analysis that considers both flow and structural motion. It can be used to dissect the flow over other actively deforming bodies to differentiate the potential role of competing modes. The energy content of the competing modes can be used to evaluate the effectiveness of different active control methods and determine the optimal geometry morphing.

Although it is shown that the observed dynamic response is robust with respect to the structural stiffness and damping values, other aspects of the active flap-foil interaction such as flap size or foil geometry require further investigation before their roles in the geometry-induced fluttering phenomena can be thoroughly explained. Another improvement would be to expand the current study to 3D setup using differential geometry techniques. Quasiconformal mapping techniques are proper candidates for shape recognition and surface mapping. Methods like the discrete conformal mapping (DCM) preserve the angle of the mesh while ensuring Laplacian conservation [59–61], which are required ingredients to extend the proposed method to three dimensions. In addition, advanced tracking techniques can be employed to handle transient deforming structures [62,63]. Finally, the proposed modal analysis can be adapted to develop reduced-order models for studying



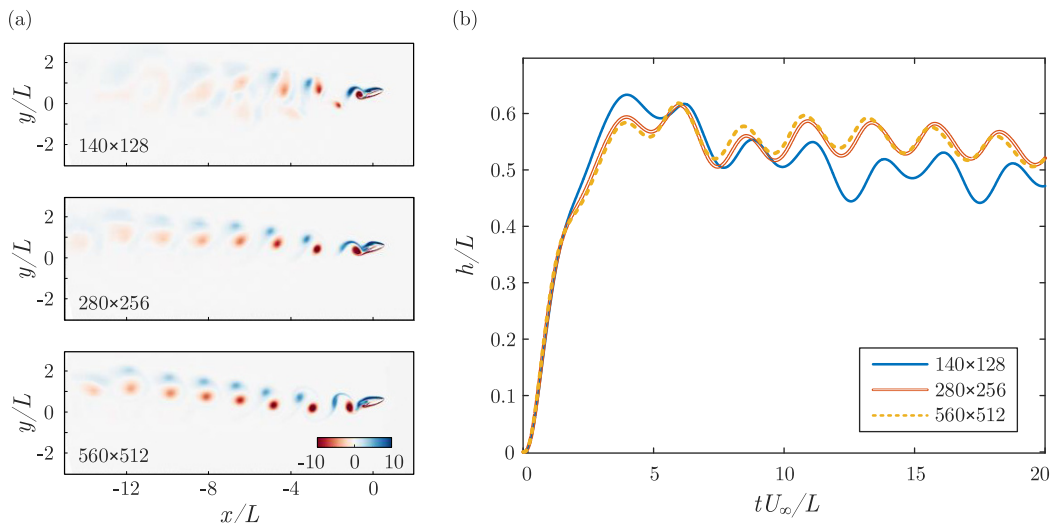


FIG. 14. (a) Instantaneous snapshot of the vorticity field with the resolution of  $140 \times 128$ ,  $280 \times 256$ , and  $560 \times 512$  in the radial and azimuthal directions, respectively. (b) Comparison of the heaving time histories with three different grid resolutions.

different control strategies for morphing systems to achieve better mobility or achieve higher energy extraction efficiency in nonuniform flow conditions.

#### ACKNOWLEDGMENTS

This study is partly supported by the Defense Advanced Research Projects Agency, Grant No. D19AP00035. The authors would also like to thank Florida State University Research Computing Center for providing the computational resources.

#### APPENDIX A: GRID REFINEMENT STUDY

A grid refinement study is performed by employing coarse ( $140 \times 128$ ), fine ( $560 \times 512$ ), and medium ( $280 \times 256$ ) grid resolutions. Figure 14(a) compares the instantaneous snapshots of these resolutions at the same time instance and the same simulation parameters ( $\text{AoA} = 20^\circ$ ,  $\theta_0 = 22.5^\circ$ ,  $A = 22.5^\circ$ ,  $\text{St}_f = 0.4$ ). Similar vortex fields are obtained for the medium and fine grids. The heaving displacement time history plotted in Fig. 14(b) confirms that the medium resolution can capture the foil movement accurately. Based on this, the medium resolution grid is selected for the current study. We refer to [41] for the validation of the algorithm.

#### APPENDIX B: EFFECT OF STRUCTURAL STIFFNESS AND DAMPING

Figure 15 shows the average heaving displacement and oscillatory amplitude for different flap frequencies and varied stiffness and damping values. As anticipated, the average heaving displacement reduces inverse proportionally with the increase of  $k_h$ . On the other hand, increasing the damping does not change the average displacement much but merely decreases the heaving amplitude. Changing the stiffness or damping does not significantly impact the dominant frequencies, implying that the flap-induced and the flow-induced vortex shedding are still the main driving force of the plunging motion. Hence, the observation discussed in the current paper could be drawn to a wide range of structural parameters. However, from the preliminary analysis, the structural properties profoundly impact the power generated when the damper is used as the energy harvesting

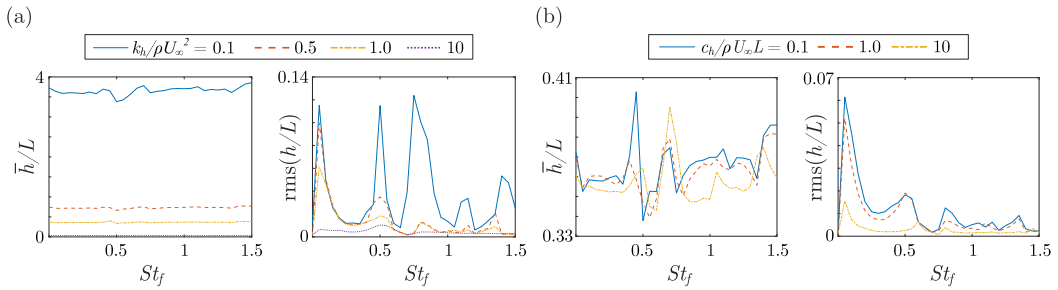


FIG. 15. The average heaving displacement and heaving amplitude of (a) varied stiffness with fixed unity damping and (b) varied damping with fixed unity stiffness.

mechanism. The subject of ongoing work is to identify optimal combinations of structural design and active control to achieve the highest energy harvesting efficiency.

- 
- [1] R. L. Bisplinghoff, H. Ashley, and R. L. Halfman, *Aeroelasticity* (Courier Corporation, North Chelmsford, MA, 2013).
- [2] A. Collar, The expanding domain of aeroelasticity, *J. Roy. Aeronaut. Soc.* **50**, 613 (1946).
- [3] M. H. Hansen, Aeroelastic instability problems for wind turbines, *Wind Energy* **10**, 551 (2007).
- [4] A. Ducoin and Y. L. Young, Hydroelastic response and stability of a hydrofoil in viscous flow, *J. Fluids Struct.* **38**, 40 (2013).
- [5] D. Poirel, V. Metivier, and G. Dumas, Computational aeroelastic simulations of self-sustained pitch oscillations of a NACA0012 at transitional Reynolds numbers, *J. Fluids Struct.* **27**, 1262 (2011).
- [6] Y. Zhu, Y. Su, and K. Breuer, Nonlinear flow-induced instability of an elastically mounted pitching wing, *J. Fluid Mech.* **899**, A35 (2020).
- [7] M. W. Kehoe, A historical overview of flight flutter testing, in *AGARD Structures and Materials Panel Meeting*, No. NASA-TM-4720 (NASA, Washington, DC, 1995).
- [8] V. Mukhopadhyay, Historical perspective on analysis and control of aeroelastic responses, *J. Guid. Control. Dyn.* **26**, 673 (2003).
- [9] R. D. Blevins, *Flow-Induced Vibration* (Van Nostrand Reinhold, New York, 1977).
- [10] M. O. L. Hansen, J. N. Sørensen, S. Voutsinas, N. Sørensen, and H. A. Madsen, State of the art in wind turbine aerodynamics and aeroelasticity, *Prog. Aerospace Sci.* **42**, 285 (2006).
- [11] O. H. Amman, T. von Kármán, and G. B. Woodruff, *The Failure of the Tacoma Narrows Bridge* (Federal Works Agency, Washington, DC, 1941).
- [12] H. L. Fierstine and V. Walters, Studies in locomotion and anatomy of scombroid fishes, *Mem. South. Calif. Acad. Sci.* **6**, 1 (1968).
- [13] M. Sfakiotakis, D. M. Lane, and J. B. C. Davies, Review of fish swimming modes for aquatic locomotion, *IEEE J. Oceanic Eng.* **24**, 237 (1999).
- [14] Q. Zhu and K. Shoele, Propulsion performance of a skeleton-strengthened fin, *J. Exp. Biol.* **211**, 2087 (2008).
- [15] P. Freymuth, Thrust generation by an airfoil in hover modes, *Exp. Fluids* **9**, 17 (1990).
- [16] H. Liu and K. Kawachi, A numerical study of insect flight, *J. Comput. Phys.* **146**, 124 (1998).
- [17] D. A. Read, F. Hover, and M. Triantafyllou, Forces on oscillating foils for propulsion and maneuvering, *J. Fluids Struct.* **17**, 163 (2003).
- [18] K. Sum Wu, J. Nowak, and K. S. Breuer, Scaling of the performance of insect-inspired passive-pitching flapping wings, *J. R. Soc. Interface* **16**, 20190609 (2019).
- [19] X. Wu, X. Zhang, X. Tian, X. Li, and W. Lu, A review on fluid dynamics of flapping foils, *Ocean Eng.* **195**, 106712 (2020).

- [20] Q. Zhu and Z. Peng, Mode coupling and flow energy harvesting by a flapping foil, *Phys. Fluids* **21**, 033601 (2009).
- [21] A. Abdelkefi, Aeroelastic energy harvesting: A review, *Int. J. Eng. Sci.* **100**, 112 (2016).
- [22] A. B. Rostami and M. Armandei, Renewable energy harvesting by vortex-induced motions: Review and benchmarking of technologies, *Renew. Sustain Energy Rev.* **70**, 193 (2017).
- [23] Q. Xiao and Q. Zhu, A review on flow energy harvesters based on flapping foils, *J. Fluids Struct.* **46**, 174 (2014).
- [24] D. Li, Y. Wu, A. Da Ronch, and J. Xiang, Energy harvesting by means of flow-induced vibrations on aerospace vehicles, *Prog. Aerospace Sci.* **86**, 28 (2016).
- [25] Y. Lee, A. Vakakis, L. Bergman, D. M. McFarland, and G. Kerschen, Suppression aeroelastic instability using broadband passive targeted energy transfers, Part 1: Theory, *AIAA J.* **45**, 693 (2007).
- [26] S. Fatimah and F. Verhulst, Suppressing flow-induced vibrations by parametric excitation, *Nonlin. Dyn.* **31**, 275 (2003).
- [27] V. Giurgiutiu, Review of smart-materials actuation solutions for aeroelastic and vibration control, *J. Intell. Mater. Syst. Struct.* **11**, 525 (2000).
- [28] S. Barbarino, O. Bilgen, R. M. Ajaj, M. I. Friswell, and D. J. Inman, A review of morphing aircraft, *J. Intell. Mater. Syst. Struct.* **22**, 823 (2011).
- [29] K. W. Moored, III and H. Bart-Smith, The analysis of tensegrity structures for the design of a morphing wing, *ASME. J. Appl. Mech.* **74**, 668 (2007).
- [30] J. J. Block and T. W. Strganac, Applied active control for a nonlinear aeroelastic structure, *J. Guid. Control. Dyn.* **21**, 838 (1998).
- [31] T. Theodorsen, General theory of aerodynamic instability and the mechanism of flutter, NACA Technical Report TR-496 (1949).
- [32] Z. Wang, A. Behal, and P. Marzocca, Model-free control design for multiinput multi-output aeroelastic system subject to external disturbance, *J. Guid. Control. Dyn.* **34**, 446 (2011).
- [33] G. Platanitis and T. W. Strganac, Control of a nonlinear wing section using leading-and trailing-edge surfaces, *J. Guid. Control. Dyn.* **27**, 52 (2004).
- [34] A. Medina, M. S. Hemati, and M. Rockwood, Separated flow response to rapid flap deflection, *AIAA J.* **58**, 1446 (2020).
- [35] H. Ohta, A. Fujimori, P. Nikiforuk, and M. Gupta, Active flutter suppression for two-dimensional airfoils, *J. Guid. Control. Dyn.* **12**, 188 (1989).
- [36] D. Tang, E. Dowell, and L. Virgin, Limit cycle behavior of an airfoil with a control surface, *J. Fluids Struct.* **12**, 839 (1998).
- [37] K. Zhang and A. Behal, Continuous robust control for aeroelastic vibration control of a 2-D airfoil under unsteady flow, *J. Vibration Control* **22**, 2841 (2016).
- [38] A. Goza and T. Colonius, Modal decomposition of fluid–structure interaction with application to flag flapping, *J. Fluids Struct.* **81**, 728 (2018).
- [39] E. Liberge and A. Hamdouni, Reduced order modelling method via proper orthogonal decomposition (POD) for flow around an oscillating cylinder, *J. Fluids Struct.* **26**, 292 (2010).
- [40] K. Menon and R. Mittal, Dynamic mode decomposition based analysis of flow over a sinusoidally pitching airfoil, *J. Fluids Struct.* **94**, 102886 (2020).
- [41] T.-K. Wang and K. Shoele, Geometrically weighted modal decomposition techniques, *J. Fluid Mech.* **911**, A41 (2021).
- [42] M. Mendez, M. Balabane, and J.-M. Buchlin, Multi-scale proper orthogonal decomposition of complex fluid flows, *J. Fluid Mech.* **870**, 988 (2019).
- [43] C. Van Dam, The aerodynamic design of multi-element high-lift systems for transport airplanes, *Prog. Aerospace Sci.* **38**, 101 (2002).
- [44] H. L. Morgan Jr., Experimental test results of energy efficient transport (EET) high-lift airfoil in Langley low-turbulence pressure tunnel, NASA Technical Memorandum, NASA/TM-2002-211780 (NASA, Washington, DC, 2002).
- [45] E. Nissim, Flutter suppression using active controls based on the concept of aerodynamic energy, NASA Technical Note, NASA-TN-D-6199 (NASA, Washington, DC, 1971).

- [46] K. Reddy, J. Chen, A. Behal, and P. Marzocca, Multi-input/multi-output adaptive output feedback control design for aeroelastic vibration suppression, *J. Guid. Control. Dyn.* **30**, 1040 (2007).
- [47] L. Guglielmini and P. Blondeaux, Propulsive efficiency of oscillating foils, *Eur. J. Mech. B* **23**, 255 (2004).
- [48] E. J. Chae, D. T. Akcabay, and Y. L. Young, Dynamic response and stability of a flapping foil in a dense and viscous fluid, *Phys. Fluids* **25**, 104106 (2013).
- [49] C. Pozrikidis, *Introduction to Theoretical and Computational Fluid Dynamics* (Oxford University Press, Oxford, 2011).
- [50] J. D. Eldredge, *Mathematical Modeling of Unsteady Inviscid Flows* (Springer, Berlin, Heidelberg, 2019).
- [51] G. Birkhoff, R. S. Varga, and D. Young, Alternating direction implicit methods, in *Advances in Computers*, edited by F. L. Alt and M. Rubinoff (Elsevier, Amsterdam, 1962), Vol. 3, pp. 189–273.
- [52] T.-K. Wang, T. Solano, and K. Shoele, Bridge the gap: correlate face mask leakage and facial features with 3D morphable face models, *J. Expo. Sci. Environ. Epidemiol.* (2021).
- [53] K. Menon and R. Mittal, Flow physics and dynamics of flow-induced pitch oscillations of an airfoil, *J. Fluid Mech.* **877**, 582 (2019).
- [54] M. La Mantia and P. Dabnichki, Added mass effect on flapping foil, *Engi. Anal. Boundary Elements* **36**, 579 (2012).
- [55] P.-F. Lei, J.-Z. Zhang, W. Kang, S. Ren, and L. Wang, Unsteady flow separation and high performance of airfoil with local flexible structure at low Reynolds number, *Commun. Comput. Phys.* **16**, 699 (2014).
- [56] G. Jones, M. Santer, and G. Papadakis, Control of low Reynolds number flow around an airfoil using periodic surface morphing: A numerical study, *J. Fluids Struct.* **76**, 95 (2018).
- [57] W. Kang, M. Xu, W. Yao, and J. Zhang, Lock-in mechanism of flow over a low-Reynolds-number airfoil with morphing surface, *Aerospace Sci. Technol.* **97**, 105647 (2020).
- [58] L. Sirovich, Turbulence and the dynamics of coherent structures. I. coherent structures, *Q. Appl. Math.* **45**, 561 (1987).
- [59] C. Gotsman, X. Gu, and A. Sheffer, Fundamentals of spherical parameterization for 3D meshes, in *ACM SIGGRAPH 2003 Papers (SIGGRAPH '03)* (ACM Press, New York, NY, 2003), pp. 358–363.
- [60] M. S. Floater and K. Hormann, Surface parameterization: A tutorial and survey, in *Advances in Multiresolution for Geometric Modelling*, edited by N. A. Dodgson, M. S. Floater, and M. A. Sabin (Springer, Berlin, Heidelberg, 2005), pp. 157–186.
- [61] H. Li and R. Hartley, Conformal spherical representation of 3D genus-zero meshes, *Pattern Recognit.* **40**, 2742 (2007).
- [62] W. Zeng and X. D. Gu, Registration for 3D surfaces with large deformations using quasi-conformal curvature flow, in *CVPR 2011* (IEEE, New York, 2011), pp. 2457–2464.
- [63] Y. T. Lee, K. C. Lam, and L. M. Lui, Landmark-matching transformation with large deformation via  $n$ -dimensional quasi-conformal maps, *J. Sci. Comput.* **67**, 926 (2016).